J Electroceram (2010) 24:205–213
DOI 10.1007/s10832-008-9559-2

Design, fabrication and finite element modeling of a new wagon wheel flextensional transducer

Manoj Narayanan · Robert W. Schwartz

Received: 13 March 2008 / Accepted: 1 December 2008 / Published online: 12 December 2008

Abstract Cymbal and moonie transducers exhibit greatly improved performance characteristics compared to a simple piezoelectric disk. This behavior is mainly due to the amplifying nature of the endcaps employed in these devices. Although these endcaps improve the displacement by amplifying the small lateral displacement associated with the d_{31} coefficient to a large axial displacement, this mechanism generates a very high tangential stress in the caps, which leads to a reduction in the efficiency of this transformation. In this paper, we report on a new end cap design, called the wagon wheel flextensional transducer, in which some of the clamping boundary conditions are eased by removing the metal in areas of high stress concentration. In the wagon wheel design, the tangential stresses are further reduced, thereby improving the efficiency of the transformation of the lateral to axial displacement, and consequently increasing the displacement response of the devices. Structural and impedance analyses of the devices were carried out using the commercially available software codes, ABAQUS and ATILA, respectively. Results reported for finite element modeling and experimental characterization suggest that these devices exhibit improved displacement characteristics compared to cymbal devices with similar dimensions.

Keywords Cymbal · Piezoelectric · Finite Element Modeling · Flextensional transducers

M. Narayanan (✉)
ES Division, Argonne National Laboratory,
Argonne, IL 60439, USA
e-mail: mnarayanan@anl.gov

R. W. Schwartz
Missouri University of Science and Technology,
Rolla, MO 65409-0840, USA
e-mail: rschwartz@mst.edu

1 Introduction

Cymbals and moonies are class V flextensional devices developed at the Pennsylvania State University in the late 1990s that have since been successfully used in many fields. Typical applications for these devices include vibration control, underwater transducers [1–8] and non-invasive drug delivery [9]. The devices, in general, consist of a piezoelectric disk poled in the thickness direction that is sandwiched between two metal endcaps. These metal endcaps serve two purposes. First, they act as a mechanical transformer, translating the small incident normal compressive stress into a large lateral tensile stress. Second, they act as an amplifier, translating the small lateral displacements associated with the d_{31} response of the piezoelectric layer into a large normal displacement.

Although the operational principle is the same for the moonie and cymbal devices, they differ considerably in the shape of their endcaps. Both types of metal end caps enclose a shallow air-filled cavity. In the case of a moonie transducer, the cavities are in the shape of a half moon, whereas cymbal are constructed using a truncated cone-shaped cavity, as illustrated in Fig. 1. In fact, the cymbal is an improved version of the moonie device and it was designed with the aid of finite element analysis (FEA), which suggested the presence of significant stress concentration in the moonie endcap just above the bonding layer. This concentration of stresses was eliminated by removing a portion of the metal above the bonding region, which resulted in a much more improved transducer design called the cymbal. Cymbals possess ~60% higher displacement response than moonies [1] and demonstrate additional advantages, such as improved manufacturability, low cost and the ability to easily tailor the resonance frequency by simply changing the cap material or dimensions [4].

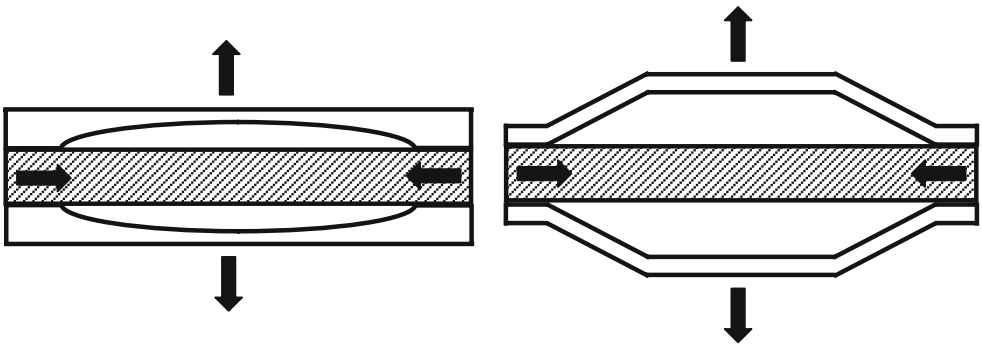

Fig. 1 Cross-sectional view of moonie (*left*) and cymbal (*right*) transducers showing the difference in the endcap shapes employed. Lateral contraction of the piezo ceramic (indicated by *horizontal arrows*) results in the axial displacement at the apex of the endcaps (indicated by *vertical arrows*)

In both of these flextensional devices, the metal caps act as mechanical transformers for converting a portion of the applied axial-direction stress into tangential and radial stresses of opposite sign [1–8]. Thus, the d_{31} and d_{33} strain coefficient responses of the PZT are additive in their contribution to the effective d_h of the device, rather than opposite in nature. Although the cymbal devices show a very large increase in displacement response (effective d_{33} ~15,000 pm/V) compared to the uncapped PZT 5A element (d_{33} ~375 pm/V) used in device fabrication, it had been reported previously that the efficiency in transforming small lateral displacements to large axial displacements is decreased because of the tangential stresses involved in this flexing mechanism [10].

In a dynamic transducer application, the resonance frequency of these devices becomes of major importance, because these devices will be driven close to this frequency to achieve high power transmission. In addition, sensors can only follow a dynamic stress or sound wave below this frequency. Therefore, in addition to understand tangential stress effects, it is also important to be able to study and predict the flextensional resonance frequency of these devices using FEA, thus realizing the full potential of these devices.

In this paper, a new endcap design, shown in Fig. 2, is proposed. Finite element analysis models suggest that this design reduces the tangential stresses in the endcaps, thereby increasing the efficiency of transformation from lateral to axial displacement. In this design, called the wagon wheel flextensional device, the stress concentration areas in the endcaps are reduced (through removing the metal by cutting pie shaped slots in those areas), thus easing the boundary conditions of the remaining areas. This design aspect alters the stress distribution compared to the original cymbal. It also reduces the fundamental resonance frequency and yields a higher displacement response compared to the standard cymbal device. The improved performance characteristics of this device, notably the reduced fundamental resonance frequency, make the device attractive for low frequency, high-power underwater projectors. Cross sectional views of wagon wheel and cymbal devices are shown in Fig. 3, along with the various dimensional parameters investigated in this research. The values of the parameters in Fig. 3 are reported in Table 1. This paper also reports on the various models created to predict the deformation and resonance frequencies of the devices using FEA.

2 Modeling

Both structural and piezoelectric modeling was carried out in this investigation. Two different software codes were used to study the proposed devices: ABAQUS (Abaqus Inc., West Lafayette, IN) used for structural modeling and ATILA (Micromechatronics Inc., State College, PA), which is specific to coupled field problems like piezoelectric, magnetostrictive, and radiation models. 3D models with the

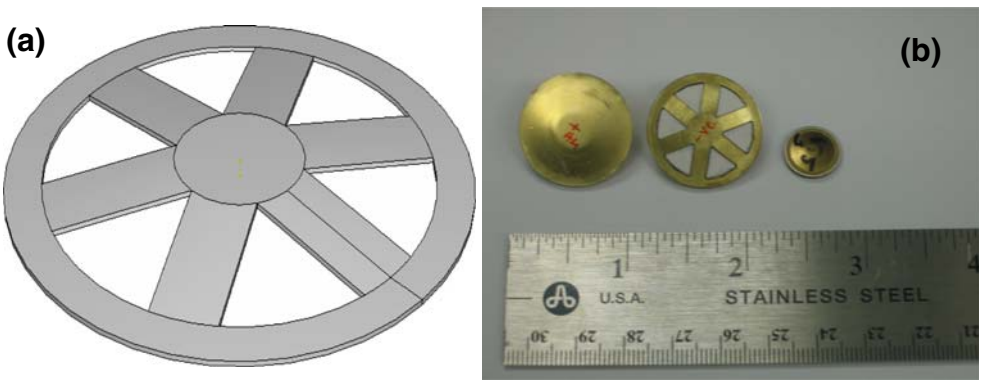

Fig. 2 (**a**) 3D view of a wagon wheel endcap and (**b**) photograph showing the cymbal (*left*), wagon wheel (*center*) and standard cymbal (*right*) transducer

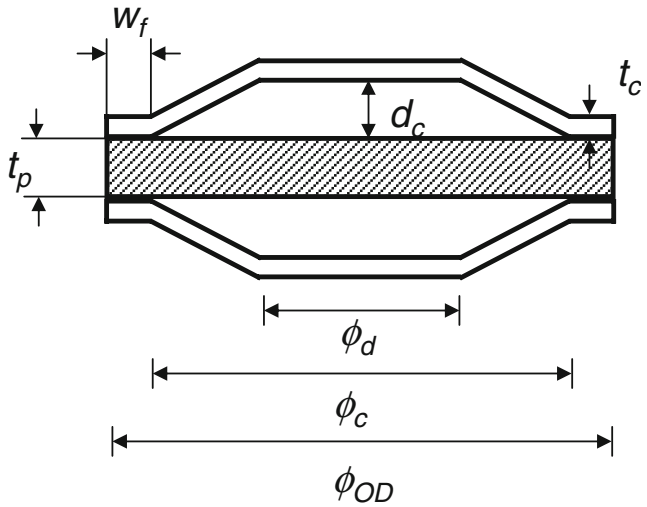

Fig. 3 Cross-section view of a cymbal and a wagon wheel device marked with the various dimensional parameters. For clarification of the dimensions refer to Table 1

necessary boundary conditions were created using the software codes and solved for the deformation, stress distribution and impedance characteristics.

2.1 Structural modeling

Structural analysis of the end caps was carried out using the ABAQUS software code, which is widely used in the field of structural and thermal simulations. For structural modeling, a 3D representation of the endcaps was created and the displacement of the apex of the endcap was simulated with uniform mechanical loading normal to the rim surface of the endcap, as illustrated in Fig. 4. The rim surface of the endcap is defined as the area obtained by the product of the outer circumference and the thickness of the metal sheet, i.e., $\pi \times \phi_{OD} \times t_c$. In this model, the flange was constrained to move in the axial direction and the load was applied perpendicular to the rim surface. Note that the coordinate system is different for the two models, i.e., displacement along the 3 direction for the cymbal model and along the 2 direction for wagon wheel model. The different choices for the coordinate systems were dictated by the different in-built functions (sweep, cut and extrude) that was used to create the endcap models with ease. The simulation boundary conditions for the cymbal and the wagon wheel endcaps are also shown in Fig. 4. The displacement at the apex is simulated for uniform loading along the rim surface. Both the Von-Mises stresses and displacement at the apex are reported from the simulations. It should also be noted that both software codes employed operate under the assumption that the material properties are linear. Separate subroutines must be written and included to account for nonlinearity in material properties.

2.2 Piezoelectric modeling

Substantial importance is given to modeling piezoelectric devices because of the ease in determining the response of a device accurately under various environmental conditions through computer simulations. PZFLEX (Weidlinger Associates Inc., Los Altos, CA), ATILA and ANSYS (Ansys Inc., Canonsburg, PA) are a few of the commercially available software packages used for simulating piezoelectric problems. All of these software codes are formulated using a set of general constitutive equations, which for a linear piezoelectric material are given in Eqs. 1a and b [11, 12]

$$\{T\} = \left[c^E\right]\{S\} - [e]^T\{E\} \tag{1a}$$

$$\{D\} = [e]\{S\} + \left[\varepsilon^S\right]\{E\} \tag{1b}$$

where $\{T\}$ is the stress tensor, $\{S\}$ the strain tensor, $\{E\}$ the electric field, $\{D\}$ the dielectric displacement, $[c^E]$ the stiffness matrix at constant electric field, $[\varepsilon^S]$ the dielectric permittivity matrix at constant strain, and $[e]$ the piezoelectric coupling coefficient tensor. Equations 1a and b are the governing equations for a general piezoelectric problem that can be reduced to the global finite element equations, in matrix form, given in Eq. 2 [13, 14].

$$\begin{bmatrix} [K_{uu}] - \omega^2[M] & [K_{u\Phi}] \\ [K_{u\Phi}]^T & K_{\Phi\Phi} \end{bmatrix} \begin{bmatrix} \underline{U} \\ \underline{\Phi} \end{bmatrix} = \begin{bmatrix} \underline{\mathrm{O}} \\ -\underline{\mathrm{q}} \end{bmatrix} \tag{2}$$

where $[K_{uu}]$ is the stiffness matrix, $[K_{u\Phi}]$ is the piezoelectric matrix, $[K_{\Phi\Phi}]$ is the permittivity matrix, $[M]$ is the consistent mass matrix, U is the displacement vector, Φ is the electrical potential vector, q is the electrical charge vector, and ω is the angular frequency.

We have modeled both the cymbal and wagon wheel devices to understand the impedance characteristics and to predict the fundamental resonance frequencies of the devices. ATILA solves Eq. 2 for modal analysis problems to determine the deformation and vibration modes of a piezoelectric structure. The harmonic behavior of the device

Table 1 Dimensions of the cymbal and wagon wheel devices.

Parameter	Wagon wheel and cymbal (mm)
Metal sheet thickness, t_c	0.25
Cavity depth, d_c	0.70
Cavity diameter at base, ϕ_c	21.0
Cavity diameter at apex, ϕ_d	7.00
Flange width, w_f	2.00
PZT thickness, t_p	1.00
PZT and endcap outer diameter, ϕ_{OD}	25.0

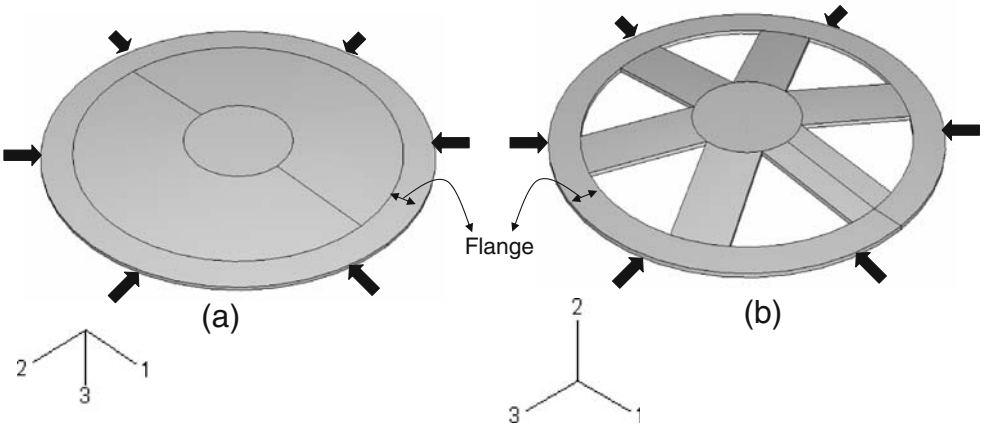

Fig. 4 Schematic showing the structural model for (**a**) cymbal and (**b**) wagon wheel endcaps. The arrows around the circumference indicate the normal load applied on the rim surface of the endcaps resulting in a axial displacement at the apex of the end cap. Note: The coordinate system is different for the models; i.e., the axial displacement is in the negative 3 direction for the cymbal and in the positive 2 direction for the wagon wheel model, for reasons noted in the text

(impedance characteristics) may be determined using ATILA by solving Eq. 2 for eigenvalues under short and open circuit boundary conditions to determine the resonance and antiresonance frequencies for different modes. The 3D models for the cymbal and wagon wheel devices were reduced to half and quarter of the actual device due to the symmetry these devices possess about the *Z*-axis and the *X*–*Y* plane, as shown in Fig. 5. Reducing the model with symmetry elements reduces the computational time and allows the use of a higher density mesh in the model, improving the accuracy of the predictions. The piezoelectric models consisted of the endcap and the piezoelectric disks and did not include the epoxy layer, as it increased the mesh size and the computational time required for solution. The different properties used in the model are reported in Table 2.

3 Experimental

3.1 Fabrication of devices

Due to the difficulty in making a wagon wheel endcap 12.7 mm in diameter with the available resources in our laboratory, which is comparable to the standard cymbal devices studied by the researchers in [1–8], a scaling factor of two was used for the devices in this research. The standard cymbal device (12.7 mm diameter), along with the devices made in this research, are illustrated in Fig. 2(b), and as noted previously, the dimensions of the wagon wheel and the cymbal device fabricated in this research are given in Table 1.

The process for cymbal and wagon wheel device fabrication is essentially the same, except for the fact that

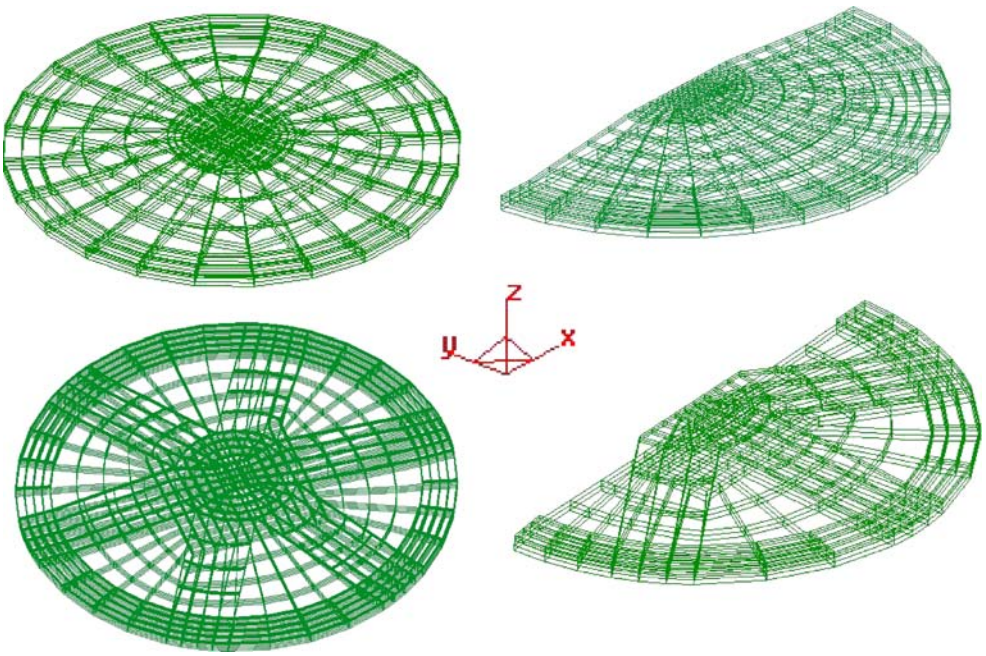

Fig. 5 Meshed view of half (*left*) and quarter (*right*) models of a cymbal (*top*) and wagon wheel device (*bottom*)

Table 2 The various properties used in the model for Brass and PKI 552 (PZT 5H).

PKI 552 (PZT 5H) [4, 15]	
ρ (kg/m^3)	7,600
$s_{11}^E \left(\times 10^{-12}\mathrm{m}^2/\mathrm{N}\right)$	15.9
$s_{12}^E \left(\times 10^{-12}\mathrm{m}^2/\mathrm{N}\right)$	−4.78
$s_{13}^E \left(\times 10^{-12}\mathrm{m}^2/\mathrm{N}\right)$	−8.45
$s_{33}^E \left(\times 10^{-12}\mathrm{m}^2/\mathrm{N}\right)$	20.2
$s_{44}^E \left(\times 10^{-12}\mathrm{m}^2/\mathrm{N}\right)$	43.5
d_{15} ($\times 10^{-12}$ m/V)	720
d_{31} ($\times 10^{-12}$ m/V)	−270
d_{33} ($\times 10^{-12}$ m/V)	550
$\varepsilon_{11}^T/\varepsilon_0$	3,400
$\varepsilon_{33}^T/\varepsilon_0$	3,300
Brass [14]	
ρ (kg/m^3)	8,270
E (GPa)	92
σ	0.33

the endcap pattern is first cut with a waterjet machine for the wagon wheel devices and the resulting pattern is then stamped with a steel die to form the truncated cone shape. The endcaps for the cymbal devices, shown in Fig. 2(b), are formed by stamping and cutting a 0.25 mm thick brass sheet in a specially designed steel die. The metal caps can be made of a variety of metals, such as brass, steel, kovar, titanium and tungsten, although brass was used in this research. The flanges of the metal endcaps were roughened with an 800 grit SiC abrasive paper and cleaned with acetone. The components of the epoxy, STYCAST (Emerson & Cuming, Billerica, MA), were mixed in a 4:1 (45LV Epoxy resin to 15LV Resin hardener) weight ratio and applied on the flanges of the endcap. A thin, uniform coating of the epoxy was then formed on the flange with a spin coater (P-6000, Integrated Technologies Inc., Acushnet, MA) using a spin speed of 4,000 rpm for 30 s. After the endcaps and electro-active ceramic disk were assembled, the composite was placed in a special holder to ensure endcap/PZT/endcap alignment and the entire assembly was maintained under a load of approximately 6,000 N for 24 h, in air at room temperature, to cure the epoxy. Finally, the devices were poled at 2 kV/mm for 5 min in silicone oil prior to characterization.

3.2 Displacement measurement

Free and loaded displacement characteristics were measured on the cymbal and wagon wheel devices using a Linear Voltage Displacement Transducer (LVDT). The LVDT used in this research, Schaevitz DC-EC50 (Measurement Specialties Inc, Hampton, VA), is operational over the displacement range ±0.050″. The free displacement was measured at the apex of the device (for both cymbal and wagon wheel) as a function of increasing and decreasing voltage. The 0.01 Hz sine wave voltage signal applied to the samples was generated with an Agilent Technologies 33120A function generator and a Trek 50/750 amplifier operated at a gain of 100:1. The electrical connection to the sample was made with alligator clips that were attached to the flanges of the sample. The amplitude of the signal was varied from 100 to 1,000 V and the displacement was measured using the LVDT described. The DC output of the LVDT was monitored on a Leader LBO-516 oscilloscope.

Displacement under load was measured for both the cymbals and the newly developed wagon wheel devices under a constant mechanical force of up to 20 N in 1 N incremental steps. A 1,000V_{pp} sine waveform was used as the drive signal and the displacement was measured using the same setup discussed above.

3.3 Impedance measurement

Impedance as a function of frequency, at 1 V, was measured with an HP 4194A Impedance/Gain-Phase analyzer over the frequency range from 0.1 to 12 kHz. Prior to the measurements, the instrument was first calibrated. The electrical leads were attached to the flanges of the endcaps to prevent damping of the flextensional mode resonance. It was found that impedance spectroscopy was sensitive to flaws in the bonding layer, misalignment of the end caps and asymmetry of the end caps. Thus, impedance spectra measurements provided a quick and easy way to judge the overall quality of a sample. From impedance analysis, information on the resonance (minimum impedance) and antiresonance (maximum impedance) frequencies for the flextensional mode was obtained, from which the effective electromechanical coupling coefficient of the cymbal and the wagon wheel devices were calculated using Eq. 3 [16–18]:

$$k^2 = 1 - \left(\frac{f_r}{f_a}\right)^2 \tag{3}$$

where k is the effective electromechanical coupling coefficient and f_r and f_a are the resonance and anti-resonance frequencies, respectively.

4 Results and discussion

4.1 Structural modeling

As discussed earlier, the structural model predicts the deformation and stress distribution of the endcaps, driven by the piezoelectric disk, under a uniform mechanical load. In this model, the flange was clamped in the axial direction (U_3=0 for cymbal and U_2=0 for wagon wheel) and a

uniform load was applied normal to the rim surface, as shown in Fig. 4, to simulate the displacement at the apex of the endcap. This structural simulation of the endcaps, with the above boundary conditions, is comparable to the scenario in which a cymbal or a wagon wheel device is driven by an electric field. That is, the actual piezoelectric problem was reduced to a structural problem by applying the appropriate boundary conditions. The only difference between this structural model and the actual device (cymbal and wagon wheel) is that the deformation of the endcaps is caused by uniform mechanical loading in the structural model, whereas an electric field applied across the piezoelectric disk produces the deformation in the actual device. It is believed that this mechanical loading on the endcap corresponds to a proportional electrical loading of the actual device for the same deformation. Although the exact correlation between the applied mechanical load on the endcaps and the electrical load on the actual device is unknown, the ratio of the displacements between the two endcap designs should be identical in the model and the actual device, because the displacement at the apex of the endcaps in the actual device is dependent on the lateral stiffness of the endcap.

The displacement at the apex for the two different endcap designs is shown in Fig. 6. It should be noted that the models have different coordinate systems, which results in different displacement signs. Therefore, only the magnitude of the displacements should be considered for comparison. It can be seen from the figures, that for the same transverse load of 0.001N, the apex of the wagon wheel displaces ~180% more than that of the cymbal endcap.

Since the waterjet nozzle had a minimum cutting radius (0.4 mm), the cut wagon wheel pattern had rounded corners near the top and base of the six legs instead of sharp corners that was modeled. So the sharp corners were rounded by filleting the corners. This predicted enhancement in displacement of the wagon wheel endcap reduced to ~100% when the sharp corners in the wagon wheel model was replaced with filleted corners. The predicted enhancement indicates that the lateral stiffness of the wagon wheel end cap is lower than that of the cymbal endcap. It can also be inferred that by releasing some of the clamping boundary conditions that exist in the cymbal devices, the lateral displacement is more efficiently transformed into axial displacement in the wagon wheel device.

The stress distribution in both endcaps for a uniform load normal to the rim surface is shown in Fig. 7. It was observed that the stress distribution changed significantly from the cymbal to the wagon wheel design. For the cymbal endcap structure, the stresses are concentrated near the inner edges of the flange and slowly decrease toward the apex. The stresses decrease by an order of magnitude from the inner edge of the flange to the apex. In contrast, in the wagon wheel endcap, the stresses decrease by two orders of magnitude from the inner edge of the flange to just above the base of the 6 legs. It is also worth noting that this decrease occurs over a very short distance in the wagon wheel compared to the cymbal device; i.e., most of the area above the flange is a low stress region in the wagon wheel endcap, whereas only the area near the apex is a low stress region in the cymbal endcap. This is one of the reasons why the wagon wheel device was predicted to have better displacement characteristics than the cymbal device.

4.2 Impedance modeling

Previously, standard cymbal devices have been modeled extensively using ANSYS [6] and ATILA [19]. It has been reported that the FFRF (First Fundamental Resonance Frequency), which is the flextensional resonance frequency, varies between 24 to 32 kHz, depending on the material used to fabricate the end caps. The in-air and underwater characteristics of both individual cymbal elements and cymbal arrays were also extensively reported in [6] and [19].

In this work, impedance spectra were simulated and experimentally measured for both cymbal and wagon wheel devices. Representative results for the cymbal device are presented in Fig. 8. The model predicts the flextensional resonance of the cymbal to be 9.76 kHz, which is close to the measured value of 9.1 kHz. Tressler [4] and Zhang et al. [19] have reported a FFRF of ≈10 kHz for a device 25.4 mm in diameter with brass endcaps, which agrees well with our simulated and measured values. The most likely reason that the measured flextensional resonance frequency

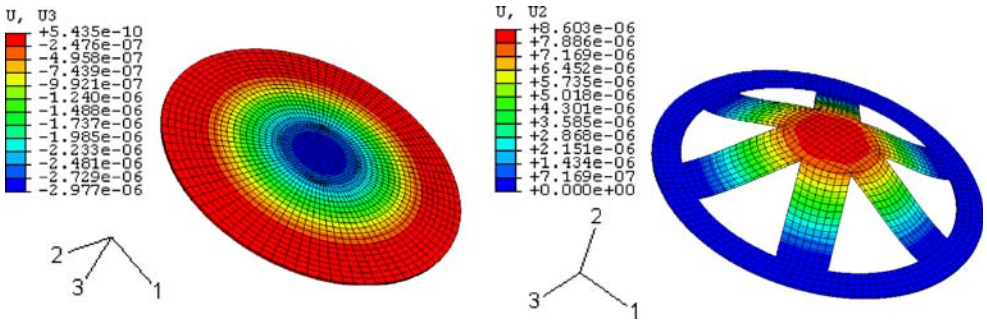

Fig. 6 Deformation of the cymbal (*left*) and wagon wheel endcap (*right*) under a uniform mechanical load along the rim. Units are in mm. Note that the coordinate system is different for the two models

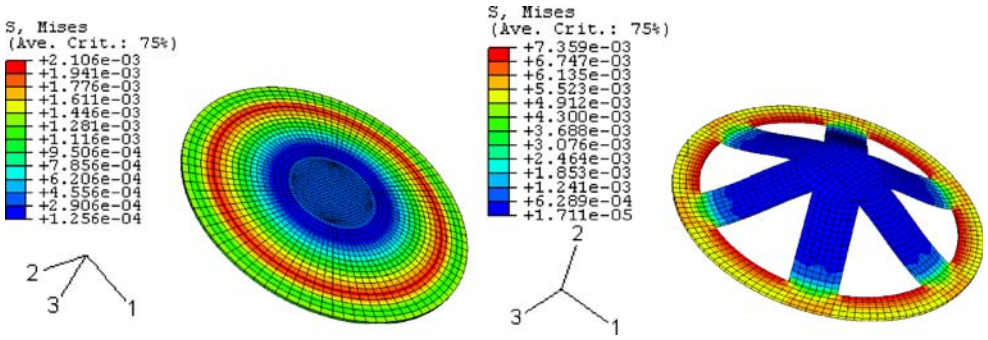

Fig. 7 Von-Mises stresses for the cymbal (*left*) and wagon wheel endcap (*right*) under a uniform mechanical load along the rim. Units are in N/mm^2 Note that the coordinate system is different for the two models

is slightly lower than the value predicted by the model is the fact that the bonding layer was not included in the model. It has been reported previously by Tressler [4] that, by the inclusion of a bonding layer in the model, the predicted flextensional resonance frequency decreases by 3–5% compared to that of a model without the bonding layer. Therefore, it is believed that the model will predict resonance frequencies closer to the actual value with the inclusion of this layer.

The predicted and experimental impedance spectra for the wagon wheel device are shown in Fig. 9. Similar to the cymbal device, the predicted flextensional resonance frequency (7.8 kHz) is higher than the measured value (7.5 kHz) for the same reason discussed above. It can be observed that the resonance frequency for the wagon wheel is lower than the analogous cymbal device. This can be explained by considering the free vibration equation where the square of the resonance frequency is directly proportional to the stiffness and inversely proportional to the mass of the structure. The mass of the wagon wheel device is lower than the cymbal, which should tend to increase the resonance frequency. Since it was observed experimentally that the wagon wheel device possessed a lower resonance frequency than cymbal, this suggests that the lateral stiffness of the wagon wheel is lower than the cymbal devices and is the more important factor in this case.

The effective electromechanical coupling coefficient is an important parameter used to compare the performance attributes of different transducers. It is defined as the square-root of the ratio of the stored mechanical energy to the input electrical energy. The effective coupling coefficients for both devices were calculated from the resonance and anti-resonance frequencies using Eq. 3 and are reported in Table 3. The experimental effective coupling coefficient of the wagon wheel is approximately 16% greater than comparable cymbal devices. This suggests that the wagon wheel device possesses lower mechanical losses and is more efficient in transforming the lateral displacement to axial displacement. The FEA model for the wagon wheel predicts effective coupling coefficients close to the experimentally determined values, although this is not the case for the cymbal devices. The model predicts a higher effective coupling coefficient for the cymbal than the wagon wheel but the measured effective coupling coefficient of the wagon wheel device is 0.22, whereas it is only 0.19 for the cymbal device. It is reasonable to believe that this is due to the non-inclusion of the epoxy layer in the model because similar discrepancies have been reported by Tressler [4].

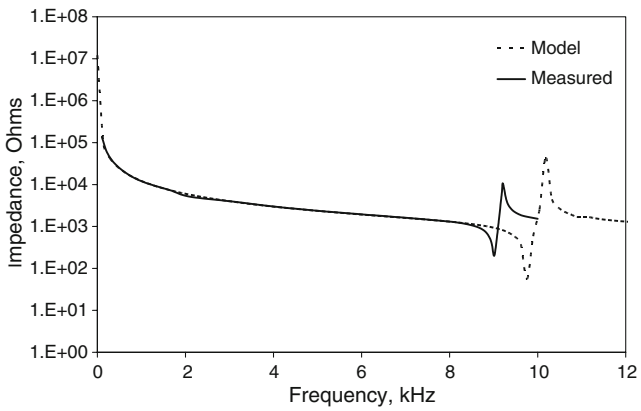

Fig. 8 Predicted and experimentally measured impedance spectra of a cymbal device showing the FFRF

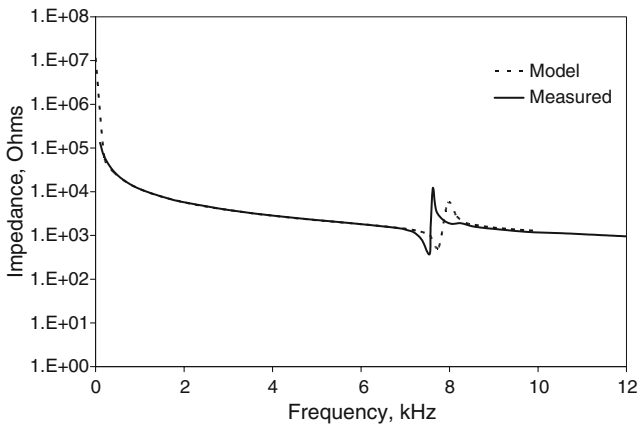

Fig. 9 Predicted and experimentally measured Impedance spectra of a wagon wheel device showing the FFRF

Table 3 Predicted and experimentally measured resonance frequencies and coupling coefficients.

	f_r FEA, kHz	f_r Experiment, kHz	k_{eff} FEA	k_{eff} Experiment
Cymbal	9.76	9.1±0.2	0.29	0.19±0.02
Wagon wheel	7.8	7.6±0.2	0.22	0.22±0.02

4.3 Free and loaded displacement

The free (zero load) displacements measured as a function of voltage for the cymbal and the wagon wheel device are shown in Fig. 10. It can be seen from the graph that the wagon wheel displaces ≈35% more than the cymbal device for the same drive voltage. This result would tend to confirm the earlier conclusion that the lateral stiffness of the wagon wheel endcap is lower than the cymbal endcap. It was noted previously in the structural modeling that the wagon wheel end cap should deform ≈100% more than the cymbal endcap, but this result was not achieved experimentally. The underlying cause of the discrepancy in the measured and predicted displacements is still unclear, although, to some extent, this inconsistency may be attributed to the fact that material non-linearity was not included in the model.

Since linearity is a very important criterion in some applications, the hysteretic behavior of the devices was studied and is also shown in Fig. 10. The degree of hysteresis (in percent) is defined as the ratio of the difference between the displacements, at half the maximum voltage, during the increasing and decreasing voltage paths and the displacement at the maximum voltage [20, 21]. It was calculated that the wagon wheel device is ≈12% hysteretic whereas the cymbal was ≈28% hysteretic. The measured value for the cymbal device fabricated in our laboratory is somewhat greater than previously reported values for these devices which range from 14 to 21% as a function of cavity depth [21]. It is believed that this is due to the fact that the devices studied in this research are larger in diameter (approximately twice) than the devices reported in [21]. The main reason for the hysteretic behavior of both the devices is irreversible domain wall motion [20]. Also, because the wagon wheel device is less hysteretic than the cymbal device, it can be concluded that the wagon wheel devices have lower mechanical losses than the cymbal devices. Stated otherwise they transfer the stresses more efficiently than the cymbals with less mechanical losses [21].

Displacement under static mechanical loads for the two different devices is compared in Fig. 11. It can be inferred from the graph that the wagon wheel device displaces more under load than the cymbal devices. For example, the wagon wheel displaces ≈102μm under a 20 N load, whereas the cymbal displaces only 67μm. This result is in general agreement with the earlier discussion that was presented regarding the energy transmission coefficients of the two devices. The wagon wheel device can do more work compared to the cymbal device for a given input electrical energy.

It may also be seen in Fig. 11 that the displacement of both devices increases with load, whereas one might expect a decrease in displacement with increasing load. It is suggested that may be due to the fact that the endcaps in both devices convert the axial compressive stress caused by loading, to lateral tensile stress, which increases the domain wall contributions to the total displacement re-

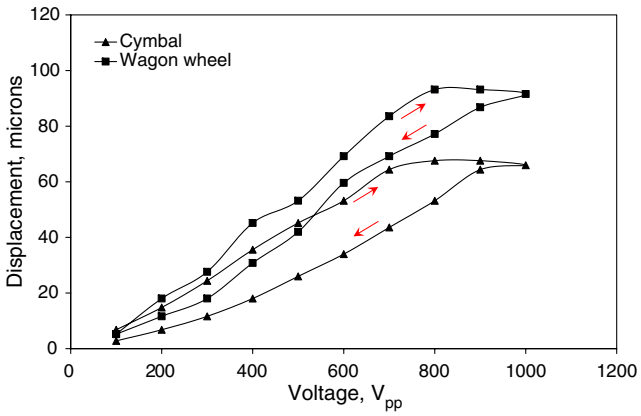

Fig. 10 Free (unloaded) displacement at the apex of the cymbal and wagon wheel devices as a function of voltage. The upper and lower half of each loop represent the increasing and decreasing voltage paths, respectively

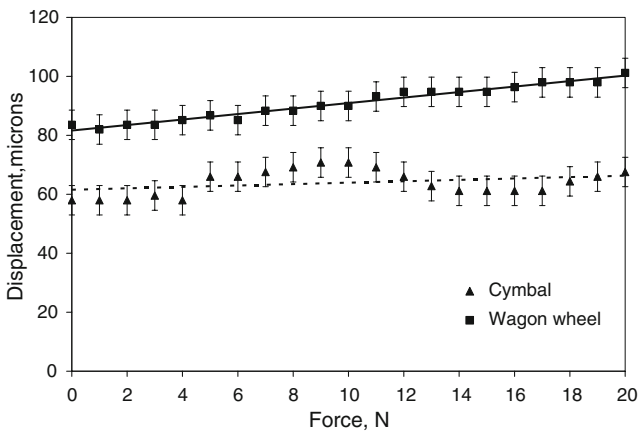

Fig. 11 Displacement at the apex of the cymbal and wagon wheel devices as a function of static mechanical load

sponse of the device. Many researchers [22–25] have previously reported on the increased domain wall contributions and strains that occur under higher lateral tensile stresses (stresses perpendicular to the poling direction), which is the principle of stress-biased actuators like Rainbow and Thunder devices. Nothwang [22] previously reported similar behavior in Thunder stress-biased actuators, where mechanically loading these devices improved their displacement characteristics.

It may also be observed in Fig. 11 that the slope of the displacement curve is higher for the wagon wheel device than the cymbal. This may suggest that domain wall contributions to performance in the wagon wheel device are greater than those in the cymbal device. This effect may also simply be due to the fact that in the wagon wheel device, the axial compressive stresses are more efficiently transformed into lateral tensile stresses.

5 Conclusions

The main goal of this study was to improve the transducer performance of existing cymbal devices by designing a new end cap in which the clamping conditions are eased, and as a result, device performance is improved. Free and loaded displacement, hysteretic behavior and device resonance frequency were experimentally measured, and impedance characteristics were correlated with predicted values from the finite element models created for these devices. The experimental first fundamental resonance frequency agreed well with the predicted values from the FEA models for both devices. It was also observed that that wagon wheel device had a lower FFRF than the cymbal device, which was attributed to the lower later stiffness of the design. The effective electromechanical coupling coefficients determined from the resonance and anti-resonance frequencies also appeared to be in agreement with the measured free and loaded displacement characteristics of the devices.

Acknowledgments The authors would like to thank Mr. John Tyler at the UMR Rock Mechanics and Explosives Research Center for cutting the wagon wheel patterns and Dr. Saikrishna Sundararaman for his comments regarding the structural modeling.

References

1. A. Dogan, K. Uchino, R.E. Newnham, ed. by C. Galassi. *Piezoelectric Materials: Advances in Science, Technology and Applications* (Kluwer, Norwell, 2000), pp. 357–374
2. R.E. Newnham, J. Zhang, R. Meyer Jr., Proc. 12th IEEE Intl. Symp. Appl. Ferro., (2001), pp. 29–32
3. A. Dogan, J.F. Fernandez, K. Uchino, R.E. Newnham, Proc. 10th IEEE Intl. Symp. Appl. Ferro. (1996), pp. 213–216
4. J. F. Tressler, Ph.D. Dissertation, The Pennsylvania State University (1997)
5. J.F. Fernandez, A. Dogan, J.T. Fielding, K. Uchino, R.E. Newnham, Sens. Actuators, A, Phys. **65**(1), 228–237 (1998) doi:10.1016/S0924-4247(97)01668-3
6. A. Dogan, E. Uzgur, D.C. Markley, R.J. Meyer, A.C. Hladky-Hennion, R.E. Newnham, J. Electroceram. **13**, 403–407 (2004) doi:10.1007/s10832-004-5132-9
7. J. Tressler, J.F. Fernandez, A. Dogan, J.T. Fielding, K. Uchino, R.E. Newnham, IEEE Ultrasonics Symp. (1995), pp. 897–900
8. A. Dogan, R.E. Newnham, U.S. Patent 5,729,077 (1998)
9. S. Lee, R.E. Newnham, N.B. Smith, IEEE Trans. UFFC **51**(2), 176–180 (2004)
10. Y. Ke, T. Guo, J. Li, IEEE Trans. UFFC **51**(9), 1171–1177 (2004)
11. R. Lerch, IEEE Trans. UFFC **37**(2), 233–247 (1990)
12. A.J. Moulson, J.M. Herbert, *Electroceramics* (Chapman and Hall, London, 1990)
13. R.J. Meyer Jr., W.J. Huges, T.C. Montgomery, D.C. Markley, R.E. Newnham, J. Electroceram. **8**, 163–174 (2002) doi:10.1023/A:1020512231158
14. ATILA® 5.2.2 User's Manual, ISEN, Lille Cedex, France (2003).
15. PKI 552 Technical data given by the manufacturer, Piezo Kinetics Inc., Bellefonte, PA 16823
16. A. Dogan, S. Yoshikawa, K. Uchino, R.E. Newnham, IEEE Ultrasonics Symp. (1994), pp. 935–939
17. J. Tressler, T. Howarth, Proc. 12th IEEE Intl. Symp. Appl. Ferro. (2001), pp. 561–564
18. J. Tressler, W. Cao, K. Uchino, R. E. Newnham, IEEE Ultrasonics Symp. (1996), 561–564
19. J. Zhang, W.J. Hughes, P. Bouchilloux, R.J. Meyer, K. Uchino, R.E. Newnham, Ultrasonics **37**, 387–393 (1999) doi:10.1016/S0041-624X(99)00021-9
20. A. Dogan, K. Uchino, R.E. Newnham, IEEE Trans. UFFC **44**(3), 597–605 (1997)
21. C.L. Sun, S.S. Guo, W.P. Li, Z.B. Xing, G.C. Liu, X.Z. Zhao, Sens. Actuators, A, Phys. **121**, 213–220 (2005) doi:10.1016/j.sna.2005.01.023
22. W.D. Nothwang, M.W. Cole, R.W. Schwartz, Int. Ferro. **71**, 207–219 (2005) doi:10.1080/10584580590964655
23. G. Li, E. Furman, G.H. Haertling, J. Am. Ceram. Soc. **80**(6), 1382–1388 (1997).
24. R.W. Schwartz, Y.W. Moon, SPIE Smart Struct. Mater. Active Mater. **4333**, 408–417 (2001)
25. X. Li, W.Y. Shih, J.S. Vartuli, D.L. Milius, I.A. Aksay, W. Shih, J. Am. Ceram. Soc. **85**(4), 844–850 (2002)